HHS Public Access

Author manuscript

Procedia Manuf. Author manuscript; available in PMC 2018 February 13.

Published in final edited form as:

Procedia Manuf. 2017 ; 10: 945–956. doi:10.1016/j.promfg.2017.07.085.

Direct Bio-printing with Heterogeneous Topology Design

AMM Nazmul Ahsan, **Ruinan Xie**, and **Bashir Khoda***

Industrial and Manufacturing Engineering, North Dakota State University, Fargo, ND, 58102, USA

Abstract

Bio-additive manufacturing is a promising tool to fabricate porous scaffold structures for expediting the tissue regeneration processes. Unlike the most traditional bulk material objects, the microstructures of tissue and organs are mostly highly anisotropic, heterogeneous, and porous in nature. However, modelling the internal heterogeneity of tissues/organs structures in the traditional CAD environment is difficult and oftentimes inaccurate. Besides, the de facto STL conversion of bio-models introduces loss of information and piles up more errors in each subsequent step (build orientation, slicing, tool-path planning) of the bio-printing process plan. We are proposing a topology based scaffold design methodology to accurately represent the heterogeneous internal architecture of tissues/organs. An image analysis technique is used that digitizes the topology information contained in medical images of tissues/organs. A weighted topology reconstruction algorithm is implemented to represent the heterogeneity with parametric functions. The parametric functions are then used to map the spatial material distribution. The generated information is directly transferred to the 3D bio-printer and heterogeneous porous tissue scaffold structure is manufactured without STL file. The proposed methodology is implemented to verify the effectiveness of the approach and the designed example structure is bio-fabricated with a deposition based bio-additive manufacturing system.

Keywords

Internal heterogeneity; Bio-modeling; bio-manufacturing; Porous internal structure

1. Introduction

Porous scaffold structures have great potential to be used as a guiding substrate for three-dimensional (3D) tissue regeneration processes. The interaction between the cells and the scaffold constitutes a dynamic regulatory system for directing tissue formation as well as regeneration in response to injury [1]. A successful interaction must facilitate the cell survival rate by cell migration, proliferation and differentiation, waste removal, and vascularization while regulating bulk degradation, inflammatory response, pH level, denaturization of proteins, and carcinogenesis affect. Inducing an amenable bio-reactor and stimulating the tissue regeneration processes while minimally upsetting the delicate equilibrium of the cellular microenvironment is the fundamental expectation of a functional

*Corresponding author. Tel.: +1-701-231-8071; fax: +1-701-231-7195. akm.khoda@ndsu.edu.

scaffold [2]. Achieving the conflicting multi-functinality through the scaffold structure will depend upon the *troika* factor, i.e., material, manufacturing processes, and its structure.

Several scaffold fabrication techniques are available and can be classified into two broad categories: i) non-Additive Manufacturing (AM), and ii) bio-AM technique. Recently bio-additive manufacturing systems have become an attractive tool for developing porous scaffolds because of the improved spatial resolutions [3, 4]. The current bio-additive manufacturing process is the surrogate of status quo AM process where STL being the *de facto* file format. The desired shape is constructed with CAD or extracted by reverse engineering process and is converted to STL-surface model and then sliced by a set of parallel planes to determine the layer contours. All the contours are planar closed curves and have the same (positive) orientation. When materials are deposited in each of these layers and stacked consecutively, a 3D scaffold is obtained. Often time, the generated model is the boundary representation (B-rep) of the targeted shape and does not capture the internal architectural information. Most of the time, the internal architecture is simplified with 'homogenization' methods. In biological systems, the pore size and structural porosity vary with tissue type, location, and function [5]. Thus, scaffolds designed with homogenous property and material distribution without considering the internal architecture do not adequately represent bio-mimicry [6–8]. Besides, the STL conversion is a surface approximation technique, which introduces loss of information in the form of chordal error, truncation error, dangling face or puncture gap in the model, and erratic nature of the model surface due to incomplete or inconsistent facet normal. Using the model with these errors will pile-up more errors in each subsequent step (build orientation, slicing, tool-path planning) of process plan. Thus there is a clear gap in the design representation of bio-scaffold models that translate to downstream inaccuracy of the bio-AM process.

Several works have been done on topology optimization techniques to design the internal architecture of porous scaffolds and implants [9, 10]. Challis *et al.* [11] optimized the porous scaffold architecture based on scaffold stiffness and diffusive transport. Dias *et al.* [12] also proposed a scaffold topology optimization algorithm for given mechanical conditions and permeability. Implicit surface modeling, which uses triply periodic minimal surfaces (TPMS), has also been employed to design porous scaffold topology design [9, 13, 14]. Thus, most of the topology design techniques create the scaffold architecture which do not mimic the original microstructure of the target area. Our focus is on designing the scaffold structure mimicking the native tissue/organ architecture and direct fabricating the structure without the use of any CAD model.

In this paper, we divided the bio-additive manufacturing process into pre-processing, processing and post-processing stage as shown in Fig. 1. Our main contribution is emphasized on the pre-processing and processing stage that deals with the design representation and the actual bio-printing. We are proposing a topology based design methodology to accurately represent the heterogeneous internal architecture tissue/organs. An image analysis technique is used that digitizes the data from bio-medical image. A weighted topology reconstruction algorithm is implemented to analyze the extrinsic property of the target area. The internal heterogeneity is then represented with parametric functions which will be used for mapping the spatial material distribution across the structure. The

generated information is directly transferred to the bio-printer and STL-free heterogeneous porous scaffold structure is manufactured.

2. Methodology

2.1. Pre-processing stage

The microstructures of tissues and organs are heterogeneous which provides multi-functionality such as mechanical, chemical, and biological. Medical images obtained from non-invasive imaging techniques, such as Computed Tomography (CT)/micro-CT/high-resolution peripheral QCT, Magnetic Resonance Imaging (MRI), or Dual-Energy X-Ray Absorptiometry (DEXA) images, can be analyzed to model the internal microstructural heterogeneity of the tissue/organ. For example, Hazrati *et. al.* [15–18] determined the bone volume fraction (BV/TV) and other microstructural parameters of bone from bone medical images using a mapping algorithm. The bone volume fraction (BV/TV) map [17], which is a measure of bone material density distribution, obtained from a CT image of the proximal portion of a femur is shown in Fig. 2(b). However, their output is not suitable for 3D bio-printing process. Hence, we develop a novel framework where the internal heterogeneity information of a tissue/organ is captured from its medical images and processed to direct 3D bio-print the tissue/organ mimicking the real one.

2.2. Medical image data digitization

Medical images (i.e., CT, MRI, DEXA, etc.) can be used as input in the proposed methodology. For the purpose of demonstration, we used a high resolution peripheral QCT image of human distal tibia [19] shown in Fig. 3(a). The medical image of tibia is, in fact, a rectangular array of pixels $\mathbf{P}_{x,y} = [P_{x,y}]$, where $P_{x,y}$ is the intensity value of a pixel at spatial location (x,y). The pixel values $P_{x,y}$ may vary spatially and are mapped as a function of x and y values. Thus the tibia image can be represented as a single valued function I:$[1, \ldots, m] \times [1, \ldots, n] \rightarrow \Re$, where m and n are the pixel numbers along X and Y directions, respectively.

The intensity values of the pixels of image I were discretized through image quantization. In this process, image I was transformed into I' :$[1, \ldots, m] \times [1, \ldots, n] \rightarrow [1, \ldots, l]$ taking only a discrete finite set of pixel values defined as quantization levels (l). This quantization level is a user defined parameter and chosen based on the complexity of the image. For instance, after quantization the scale tibia image was discretized into 8 quantization levels ($l = 8$) as shown in Fig. 3. Image Quantization was performed to consolidate the continuous pixel values into a finite discrete levels so that the pixels having intensity values closer to each other could be identified. This resulted in a set of discrete iso-intensity value regions in the image. In fact, an iso-intensity pixel value region in an image can be assumed to possess approximately same microstructural heterogeneity.

Next, the average pixel values $\overline{P}_x = \frac{1}{N_y}\sum_y P'_{x,y}$ and $\overline{P}_y = \frac{1}{N_x}\sum_x P'_{x,y}$ of the quantized image I' were determined along both X and Y directions, respectively, resulting in $\overline{\mathbf{P}}_x = \{\overline{P}_x\}$ and $\overline{\mathbf{P}}_y = \{\overline{P}_y\}$ which are plotted with respect to vertical and horizontal axis as shown in Fig. 4.

2.3. Topology reconstruction with parametric function

The internal heterogeneous architecture is represented with parametric function to reconstruct the topology for fabrication (processing stage). Adaptively segmented but connected parametric polynomial B-spline curves $\{\mathbf{C}(u)\}$ is fitted to correlate the average pixel values. The B-spline curve is a generalization of the Bézier curve, i.e., Bézier curve is a B-spline with no interior knots [20]. A Bézier curve of degree n is given by Eq.(1) where $\{B_{i,n}(u)\}$ is the n^{th} degree Bernstein polynomials.

$$\mathbf{C}(u)=\sum_{i=0}^{n} B_{i.n}(u)\mathbf{P}_i, \quad u \in [0,1]$$

$$\text{where,} \quad B_{i,n}(u)=\frac{n!}{i!(n-i)!}u^i(1-u)^{n-i} \tag{1}$$

Here, $\{\mathbf{P}_i\}_{i=0,\ldots,n}$ are the control points of the Bézier curve $\mathbf{C}(u)$. In this paper, the control points of the Bézier curve are defined by the ordered pairs of pixel location and pixel value, i.e., $\{\mathbf{P}_i = (x, \bar{P}_x)_i\}$. In order to capture the correlation between the pixel values and pixel locations along X direction, the data points $\mathbf{XP} = \{(x,\bar{P}_x)_j : j = 0,1, \ldots, (N-1)\}$ are adaptively segmented. First, an initial control point segment is formed by taking a subset $\mathbf{SXP}_{g=0} \subseteq \mathbf{XP}$ having a given cardinality $s := n+1$. Thus the initial segment can be defined as $\mathbf{XP} \supseteq \mathbf{SXP}_{g=0} = \{(x,\bar{P}_x)_j : (x,\bar{P}_x)_j \in \mathbf{XP}, j = ng, \ldots, n(g+1)\}$. Now a n^{th}-degree Bézier curve $\mathbf{C}(u)_g^x$ is fitted for this segment containing $n+1$ number of control points and the curve fitting error is evaluated using Eq. (2).

$$E=\left(\frac{1}{n+1}\right)\sum_{i=0}^{n}\left\|(x,\overline{P}_x)_i - C(u_i)\right\|^2 \tag{2}$$

Eq. (2) determines the average of the squared Euclidean distance between the control point and its corresponding point on the fitted curve. Thus, E measures the average of the total accumulation of squared distances in the segment.

Based on the value of E, the adaptive segmentation is performed. In the adaptive segmentation, the value of E is compared to a given threshold value E_{thr}. If E is greater than E_{thr}, the next segment of cardinality $n+1$ is formed as $\mathbf{XP} \supseteq \mathbf{SXK}_{g=1} = \{(x,\bar{P}_x)_j : (x,\bar{P}_x)_j \in \mathbf{XP}, j = ng, \ldots, n(g+1)\}$ and a n^{th} −degree Bézier curve $\mathbf{C}(u)_g^x$ is fitted. Note that the last point of g^{th} segment ($\mathbf{SXP}_g$) is the first point of $(g+1)^{\text{th}}$ segment ($\mathbf{SXP}_{g+1}$), ensuring the connectivity between the Bézier curves.

Algorithm 1

FitParametricCurve

Input : Control points **XP** = {(x, P_x)}, error threshold E_{thr}, initial segment size s.

Output: Set of fitted parametric curves **C** = {$\mathbf{C}(u)^x$}.

C ← ∅;
SXP ← ∅;
Q ← ∅;
$\overline{\mathbf{Q}}$ ← **XP**;
$u \in [0, 1]$;
while $|Q| < |XP|$ **do**
    SXP ← {(x, P_x)$_j$: (x, P_x)$_j \in \overline{\mathbf{Q}}$, $j = 1, \ldots, s-1$};
    $\mathbf{C}(u)^x \leftarrow \Sigma\ B(u)\mathbf{SXP}$;
    $E \leftarrow Error(\mathbf{SXP}, \mathbf{C}(u)^x)$;
    Q ← **Q** ∪ **SXP**;
    $\overline{\mathbf{Q}}$ ← $\overline{\mathbf{Q}}$ \ **SXP**;
    while $E < E_{thr}$ ***and*** $|Q| < |XP|$ **do**
        SXP ← **SXP** ∪ {(x, P_x)$_j$: (x, P_x)$_j \in \overline{\mathbf{Q}}$, $j = 1, \ldots, s-1$};
        $\mathbf{C}(u)^x \leftarrow \Sigma\ B(u)\mathbf{SXP}$;
        $E \leftarrow Error(\mathbf{SXP}, \mathbf{C}(u)^x)$;
        Q ← **Q** ∪ **SXP**;
        $\overline{\mathbf{Q}}$ ← $\overline{\mathbf{Q}}$ \ **SXP**;
    end
    C ← **C** ∪ $\mathbf{C}(u)^x$;
end
return C

However, if E is smaller than E_{thr}, instead of forming a new segment, the initial segment is updated by adding the immediate next t number of points form **XP** to $\mathbf{SXP}_{g=0}$. The updated segment becomes

$$\mathbf{SXP}'_{g=0} = \mathbf{SXP}_{g=0} \cup \{(x, \overline{P}_x)_k : (x, \overline{P}_x)_k \in \mathbf{XP}, k = n(g+1)+1, \ldots, n(g+1)+t, t \leq n+1\}.$$

Again a new $(n+t)^{\text{th}}$ −degree Bézier curve $\mathbf{C}(u)^x_g$ is fitted for updated initial segment containing $n+1$ number of control points and the curve fitting error is evaluated using Eq. (2). This process is repeated until all the points in **XP** are visited, resulting in a set of Bézier curves {$\mathbf{C}(u)^x$}. The pseudo-code for the entire process is given by Algorithm 1.

Similarly, another set of Bézier curves {$\mathbf{C}(u)^y$} is fitted through the control points **YP** = $\{(y, \overline{P}_y)_k : k = 0,1, \ldots, (M-1)\}$ to capture the correlation between the pixel values and pixel locations along Y direction. Here, M is the number of pixels along Y direction. Figure 4 demonstrates the $\overline{P}_x$ vs. X and $\overline{P}_y$ vs. Y scatter plot with Bézier curve fitting is two orthogonal directions respectively, for the tibia shown in Fig. 3. These segmented functions represent the spatial topology information for the scaffold internal architecture.

2.4. Material mapping with bi-layer function

The topology information extracted in the previous section needs to be converted into bio-printing process plan information. A layer-by-layer material deposition plan is derived using the parametric functions obtained in the previous section. In order to achieve the porous internal architecture, the internal structure of bio-models are fabricated by depositing cylindrical micro-filaments parallel to each other in every layer using a certain lay-down pattern with orientation angle θ as shown in Fig. 5. Here, the orientation angle θ defines the angle between the filaments of two consecutive layers.

The porosity of the internal architecture is computed using a unit cell representation [21] shown in Fig. 5. The unit cell is the repetitive element across the entire structure. It is assumed that the height of the unit cell is twice the layer thickness resulting in a bi-layer representation. Thus, in the unit cell, the filaments of one layer make an angle θ with the filaments of the other layer. The porosity of a unit cell can be defined based on the ratio of void space volume to the total volume of the unit cell. Considering a given zigzag laying pattern and a filament diameter, the filament spacing can be determined using Eq. (3).

$$L=\frac{\pi D(1+\frac{1}{\sin\theta})}{8(1-p)} \quad (3)$$

Here, L is the space between filaments, D is the diameter of the filaments, and θ is the bi-layer filament orientation angle. For 0°–90° zigzag filament laying pattern, θ will be 90°. Therefore, to determine the variational filament spacing $\{L_x\}$ along X direction, at the beginning when $x = 0$, $\hat{P}_{x=0}$ was predicted from the fitted Bézier curves $\{\mathbf{C}(u)^x\}$. Then the predicted pixel value $\hat{P}_{x=0}$ was fed into Eq. (4) to determine the spacing ($L_{x=0}$) between first and second filaments. Next, the value of x was updated to $L_{x=0}$. $\hat{P}_x$ was again predicted using $\{\mathbf{C}(u)\}^x\}$ and the spacing between second and third filaments were determined from Eq. (3). This process was repeated until the entire layer was covered. Algorithm 2 gives the pseudo-code for determining the variational filament spacing along the vertical X direction. The variational filament spacing $\{L_y\}$ along the orthogonal direction were also determined using $\{\mathbf{C}(u)^y\}$. Therefore, Eq. (3) can be modified to Eq. (4) in order to determine the effective porosity of a cell when $\theta = 90°$.

$$p=1-\frac{\pi D(J_x+L_y)}{8L_xL_y} \quad (4)$$

Algorithm 2

DetetinineFilainentSpacingAlongX

Input : filament radius r, $(\mathbf{C}(u)^x\}$, external contour bottom-left extreme point (X_{min}, Y_{min}), external contour bottom-right extreme point (X_{min}, Y_{min}).

Output: Set of filament spacings along X direction.

1 $L_x \leftarrow \varnothing$;

```
x ← ∅;
while x < ‖(X_max, Y_min) − (X_min, Y_min)‖ do
    P̂_x ← {C(u)^x};
    l_x ← πr/2(P̂_x); //filament spacing
    L_x ← L_x ∪ {l_x};
    x ← x + l_x;
end
return L_x
```

The outcome of the above algorithms will generate a set of sequential tool-path points for the corresponding image-layer. The chronological bottom-up or top-down visit to each layer of the object will result in sequential tool-path points for the targeted 3D scaffolds. Once all the sequential points are determined, the information is stored in a hierarchical order as a generic digital file format discussed in our previous work [22]. To construct the heterogeneous topology in the scaffold with any bio-additive manufacturing equipment, the digital structured data needs to be converted into the controller specific language. A common API (Application Program Interface) platform is also proposed, which can access and generate machine readable file for different existing bio-printers. The metadata section of the file will assure the readability by different existing bio-printing interpreters.

3. Processing/Bio-printing

An extrusion-based, bio-compatible, layered fabrication system has been designed and developed in our laboratory to deposit both engineering materials as well as delicate biomaterials with 5 μm spatial resolution. Our in house, 3D micro-nozzle biomaterial deposition system (Fig. 6) has been used to fabricate 3D scaffold structure with sodium alginate based hydrogel bio-ink [2, 6, 8] and $CaCl_2$ solution as the “cross-linker”. Sodium alginate, a type of hydrogel widely used in cell immobilization, cell transplantation, and tissue engineering, is preferred as biomaterial due to its biocompatibility and formability. The bio-ink will be filled in a reservoir, and a pneumatic system will be deployed to flow the solution via the micronozzles (100–250 μm). The system will operate at room temperature under low pressure (0–8 psi). We will dispense the calcium chloride solution onto printed sodium alginate structure through a second nozzle to provide cross-linking between the alginate anions and the calcium cations to form the hydrogel.

4. Implementation

In this study, we used de-identified CT scan stack of images of vertebra from the department of radiology, Sanford health clinic, Fargo, North Dakota. Because tissue/organ microstructural heterogeneity is modeled for bio-additive manufacturing, the CT scan sequential image slices were used to generate the layer geometries. The heterogeneity information in each layer is extracted from the CT scan through image analysis which is discussed in the following section.

The heterogeneous porosity of each layer was also modeled from the CT scan sequential images slices as discussed in sections 2. Figure 7 shows the quantized images of two vertebra slices and Fig. 8 shows the parametric curve fitting to the image information of these vertebra slices.

Once the parametric Bézier curves were fitted to map the internal architectural property of vertebra, bi-layer unit cell based layer by layer filament deposition toolpath was generated to achieve the porous heterogeneous structure of the vertebra model. A bi-layer heterogeneous/variational porosity toolpath for the first slice of the vertebra structure is shown in Fig. 9(a). Although the variational porosity across the design shown in Fig. 9(a) is not clearly visible, its variational porosity distribution can be observed by its porosity map shown in Fig. 9(b). To examine the effectiveness of our proposed method, we compared it with the conventional uniform porous structure as shown in Fig. 9. The uniform porous structure design has the overall average porosity of the first vertebra slice. Five corresponding cells were randomly chosen from both design and the porosity values were calculated. The calculated porosity values of both design are compared the real porosity from the image data digitization. Table 1 gives the percentage error of porosity between the proposed design and real image as well as the uniform design with real image. The resultant error will depends upon the layer image and distribution of porosity. With larger porosity variation within the layer will differentiate the error significantly.

The generated filament deposition toolpaths are converted into sequential machine movement instructions and sent to the machine to direct print the scaffold. The variational porosity design of the first vertebra slice presented in Fig. 9(a) is fabricated with our in house bio-printer and shown in Fig. 10. Due to the given resolution of our bio-printer, the toolpath is reconstructed (Fig. 10(a)) for larger diameter filament following the same heterogeneous design given in Fig. 9(a). Then we compared the fabricated bilayer with the design to determine the deviation the printing process. In order to do so, ten corresponding cells were randomly taken over both design and fabricated bi-layers at the same locations. The characterization of the fabricated bi-layer was performed using ImageJ software. The cell porosities of the design are calculated using Eq. (4). The unit cell comparison of the fabricated model with the designed model is shown in Table 2. The %error in the cell parameters given in Table 2 are the average %error of the ten randomly selected cells. Table 2 indicates that fabricated model is close to the designed one. The %error in the fabricated bi-layer can be attributed to several factors such as fabrication system, material property, imaging etc.

5. Conclusion

In the process of bio-fabrication, the generated bio-models with boundary representation (B-rep) or surface tessellation (mesh) do not capture the internal architectural information. In biological systems, the internal heterogeneous porosity can vary with tissue type, location, and functionality. Therefore, this paper proposes a novel methodology of topology based internal structure design to accurately represent the heterogeneous internal architecture of bio-models. The proposed methodology extracts the heterogeneity information from medical images which was used for direct bio-printing of heterogeneous tissues/organs. This

methodology is not restricted to image type (grayscale/color), equipment type, image intensity etc. However, testing the robustness of our approach for grayscale and color images of the same target area can be a future work of this research. *In vitro* cell modularization and cell viability testing on our 3D bio-printed heterogeneous structures is an intriguing subject for future investigation of this research as well.

Acknowledgments

Partial financial support provided by the National Institute of Health under COBRE: Center of Diagnostic and Therapeutic Strategy in Pancreatic Cancer (CDTSPC) Grant # P20GM109024 is acknowledged.

References

1. Khetan S, Burdick JA. Patterning hydrogels in three dimensions towards controlling cellular interactions. Soft Matter. 2011; 7:830–838.
2. Khoda AKM, Ozbolat IT, Koc B. Designing heterogeneous porous tissue scaffolds for additive manufacturing processes. Computer-Aided Design. 2013; 45:1507–1523.
3. Bettinger CJ, Weinberg EJ, Kulig KM, Vacanti JP, Wang Y, Borenstein JT, Langer R. Three-Dimensional Microfluidic Tissue-Engineering Scaffolds Using a Flexible Biodegradable Polymer. Advanced Materials. 2006; 18:165–169.
4. Khoda A, Ozbolat IT, Koc B. A functionally gradient variational porosity architecture for hollowed scaffolds fabrication. Biofabrication. 2011; 3:1–15.
5. Bartolo P, Kruth J-P, Silva J, Levy G, Malshe A, Rajurkar K, Mitsuishi M, Ciurana J, Leu M. Biomedical production of implants by additive electro-chemical and physical processes. CIRP Annals - Manufacturing Technology. 2012; 61:635–655.
6. Khoda AB, Koc B. Designing Controllable Porosity for Multifunctional Deformable Tissue Scaffolds. Journal of Medical Devices. 2012; 6:031003.
7. Sobral JM, Caridade SG, Sousa RA, Mano JF, Reis RL. Three-dimensional plotted scaffolds with controlled pore size gradients: Effect of scaffold geometry on mechanical performance and cell seeding efficiency. Acta biomaterialia. 2011; 7:1009–1018. [PubMed: 21056125]
8. Khoda AKMB, Ozbolat IT, Koc B. Engineered Tissue Scaffolds With Variational Porous Architecture. Journal of Biomechanical Engineering. 2011; 133:011001. [PubMed: 21186891]
9. Giannitelli SM, Accoto D, Trombetta M, Rainer A. Current trends in the design of scaffolds for computer-aided tissue engineering. Acta Biomaterialia. 2014; 10:580–594. [PubMed: 24184176]
10. Wang X, Xu S, Zhou S, Xu W, Leary M, Choong P, Qian M, Brandt M, Xie YM. Topological design and additive manufacturing of porous metals for bone scaffolds and orthopaedic implants: A review. Biomaterials. 2016; 83:127–141. [PubMed: 26773669]
11. Challis VJ, Roberts AP, Grotowski JF, Zhang L-C, Sercombe TB. Prototypes for Bone Implant Scaffolds Designed via Topology Optimization and Manufactured by Solid Freeform Fabrication. Advanced Engineering Materials. 2010; 12:1106–1110.
12. Dias MR, Guedes JM, Flanagan CL, Hollister SJ, Fernandes PR. Optimization of scaffold design for bone tissue engineering: A computational and experimental study. Medical Engineering & Physics. 2014; 36:448–457. [PubMed: 24636449]
13. Yoo D-J. Computer-aided porous scaffold design for tissue engineering using triply periodic minimal surfaces. International Journal of Precision Engineering and Manufacturing. 2011; 12:61–71.
14. Yoo D-J. New paradigms in cellular material design and fabrication. International Journal of Precision Engineering and Manufacturing. 2015; 16:2577–2589.
15. Hazrati Marangalou J, Ito K, van Rietbergen B. A new approach to determine the accuracy of morphology–elasticity relationships in continuum FE analyses of human proximal femur. Journal of Biomechanics. 2012; 45:2884–2892. [PubMed: 23017379]

16. Hazrati Marangalou J, Ito K, Cataldi M, Taddei F, van Rietbergen B. A novel approach to estimate trabecular bone anisotropy using a database approach. Journal of Biomechanics. 2013; 46:2356–2362. [PubMed: 23972430]
17. Hazrati Marangalou J, Ito K, Taddei F, van Rietbergen B. Inter-individual variability of bone density and morphology distribution in the proximal femur and T12 vertebra. Bone. 2014; 60:213–220. [PubMed: 24370733]
18. Hazrati Marangalou J, Eckstein F, Kuhn V, Ito K, Cataldi M, Taddei F, van Rietbergen B. Locally measured microstructural parameters are better associated with vertebral strength than whole bone density. Osteoporosis International. 2014; 25:1285–1296. [PubMed: 24306231]
19. Krug R, Burghardt AJ, Majumdar S, Link TM. High-Resolution Imaging Techniques for the Assessment of Osteoporosis. Radiologic Clinics of North America. 2010; 48:601–621. [PubMed: 20609895]
20. Piegl, L., Tiller, W. THE NURBS BOOK. 2. Springer-Verlag; Berlin Heidelberg: 1997.
21. Khoda AKMB, Ozbolat IT, Koc B. Engineered Tissue Scaffolds With Variational Porous Architecture. Journal of Biomechanical Engineering. 2010; 133:011001–011001.
22. Habib MA, Khoda B. Attribute driven process architecture for additive manufacturing. Robotics and Computer-Integrated Manufacturing. 2017; 44:253–265.

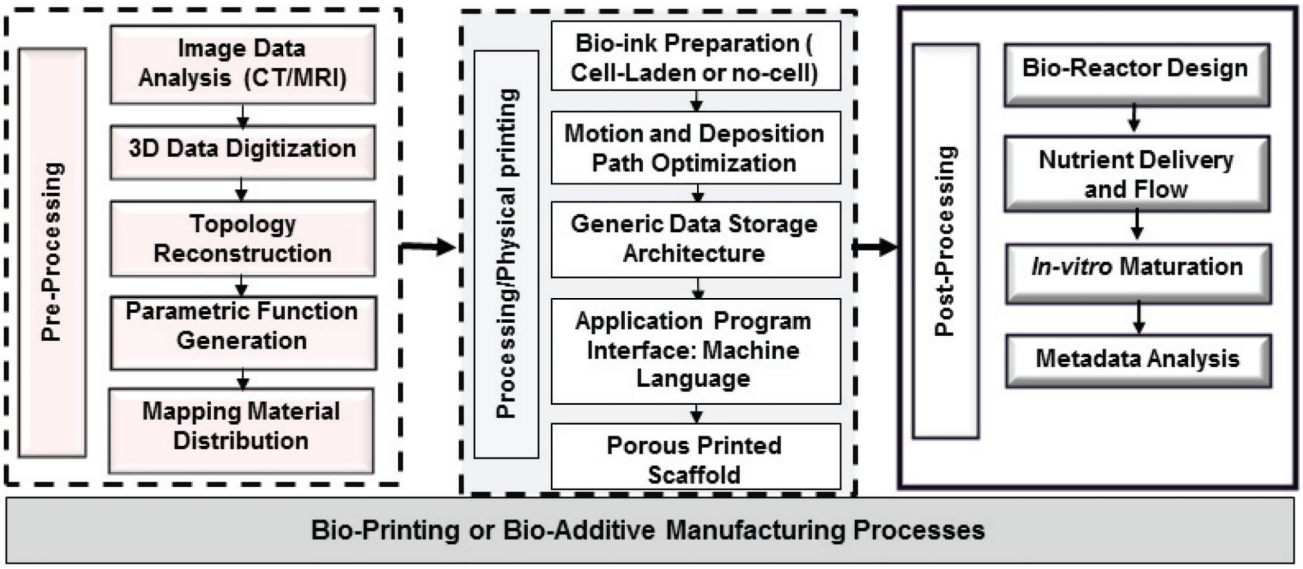

Fig. 1.
Framework of bio-additive manufacturing process.

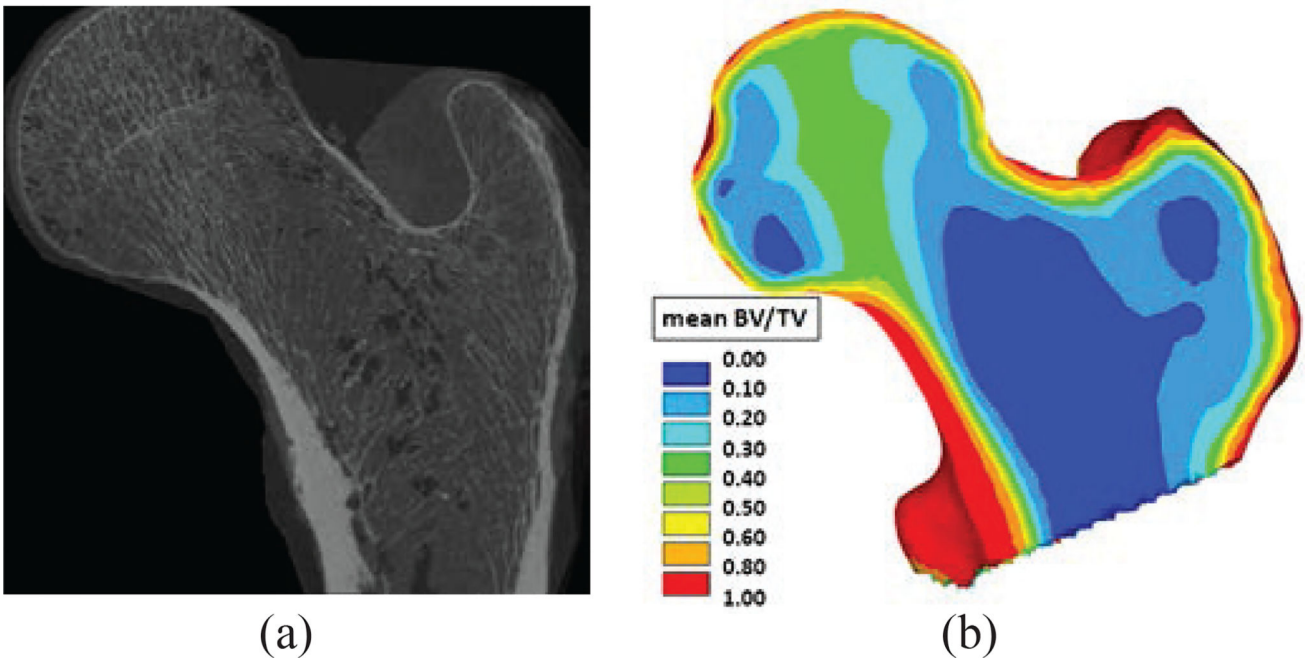

Fig. 2.
(a) Proximal femur (midcoronal plane) CT image and (b) bone volume fraction (BV/TV) [17].

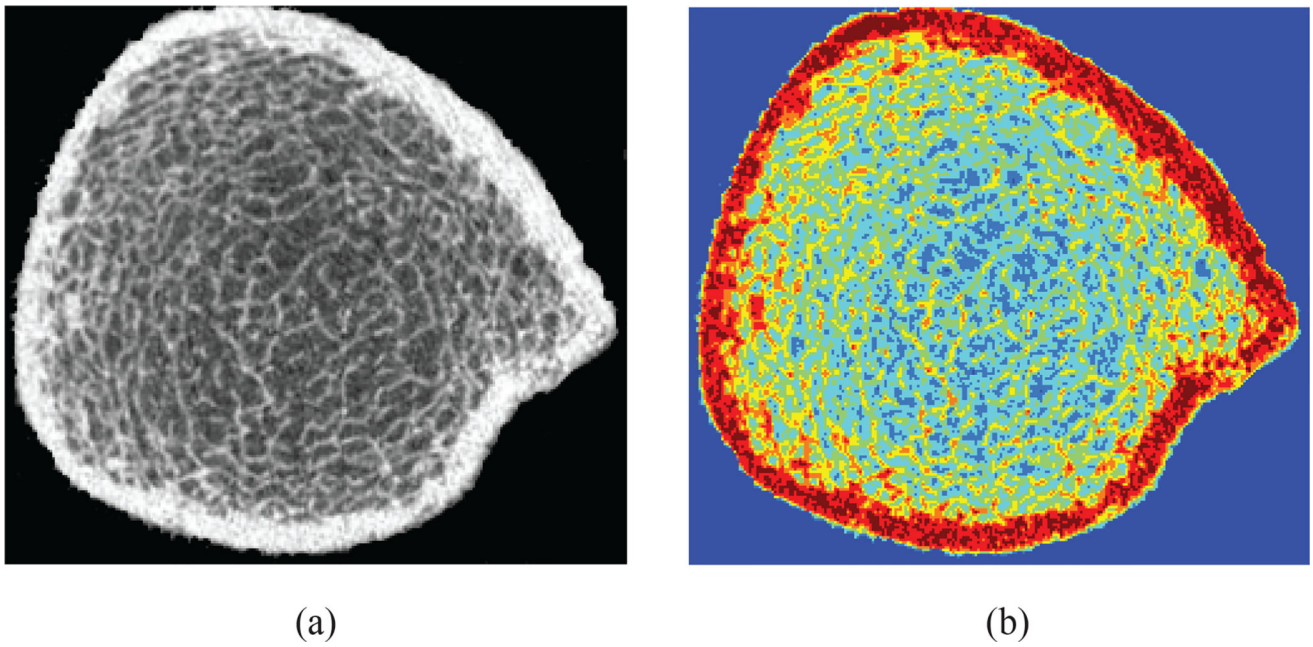

Fig. 3.
(a) High resolution peripheral QCT (HR-pQCT) image of human distal tibia [19] and (b) corresponding quantized image of the human distal tibia.

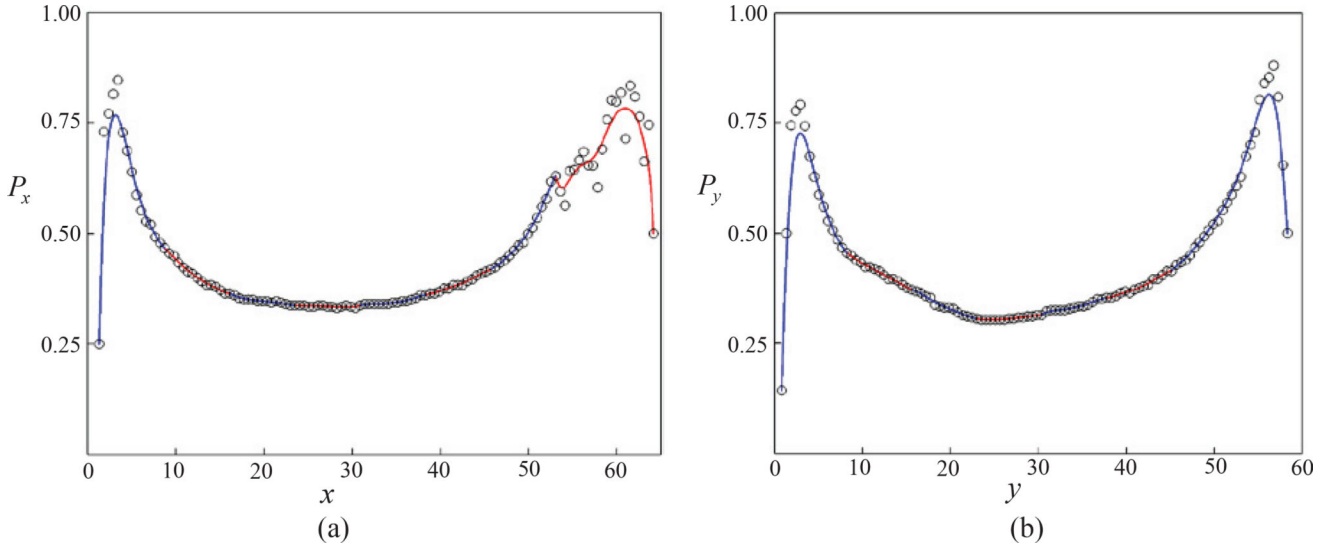

Fig. 4.

Normalized average pixel value as a function of pixel location along (a) vertical direction and (b) horizontal direction and corresponding segmented Bézier curve fitting with continuity.

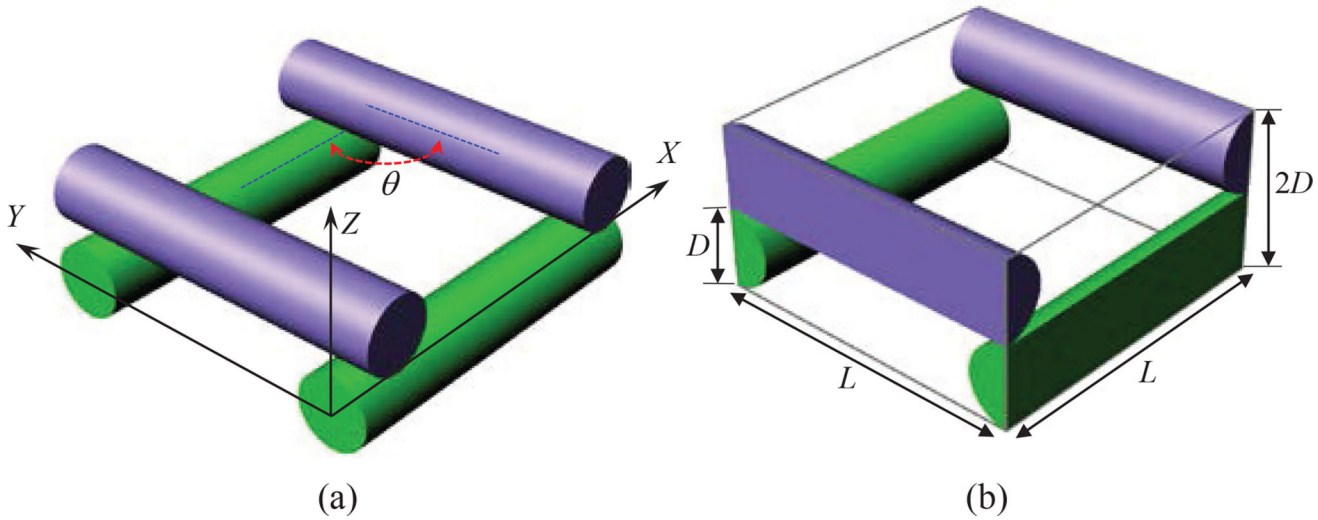

Fig. 5.
Bi-layer unit cell representation: (a) a segment of a bi-layer and (b) a unit cell

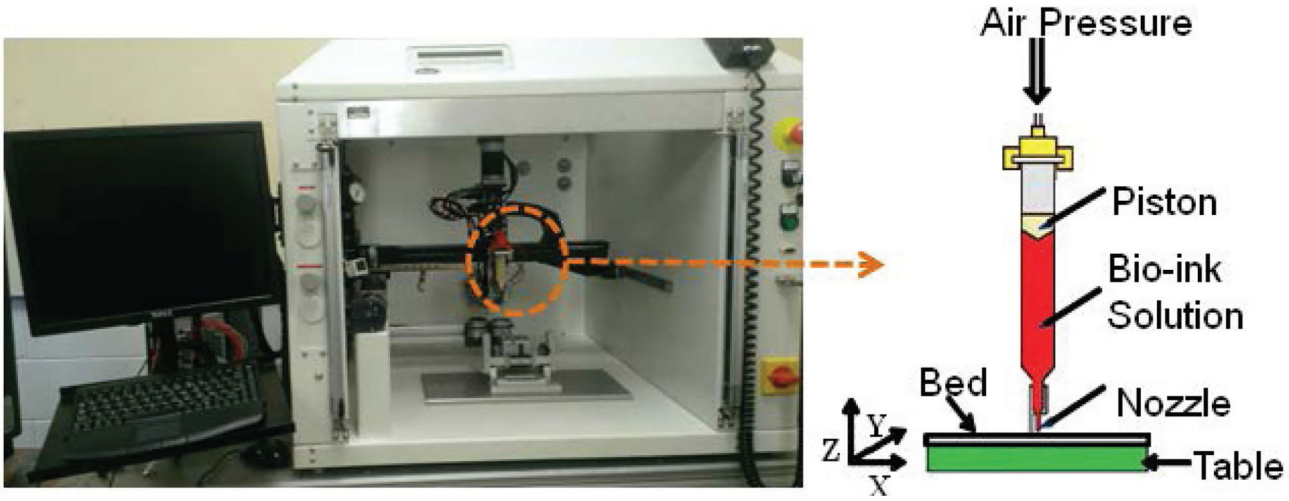

Fig. 6.
Micro-nozzle bio-additive material deposition system.

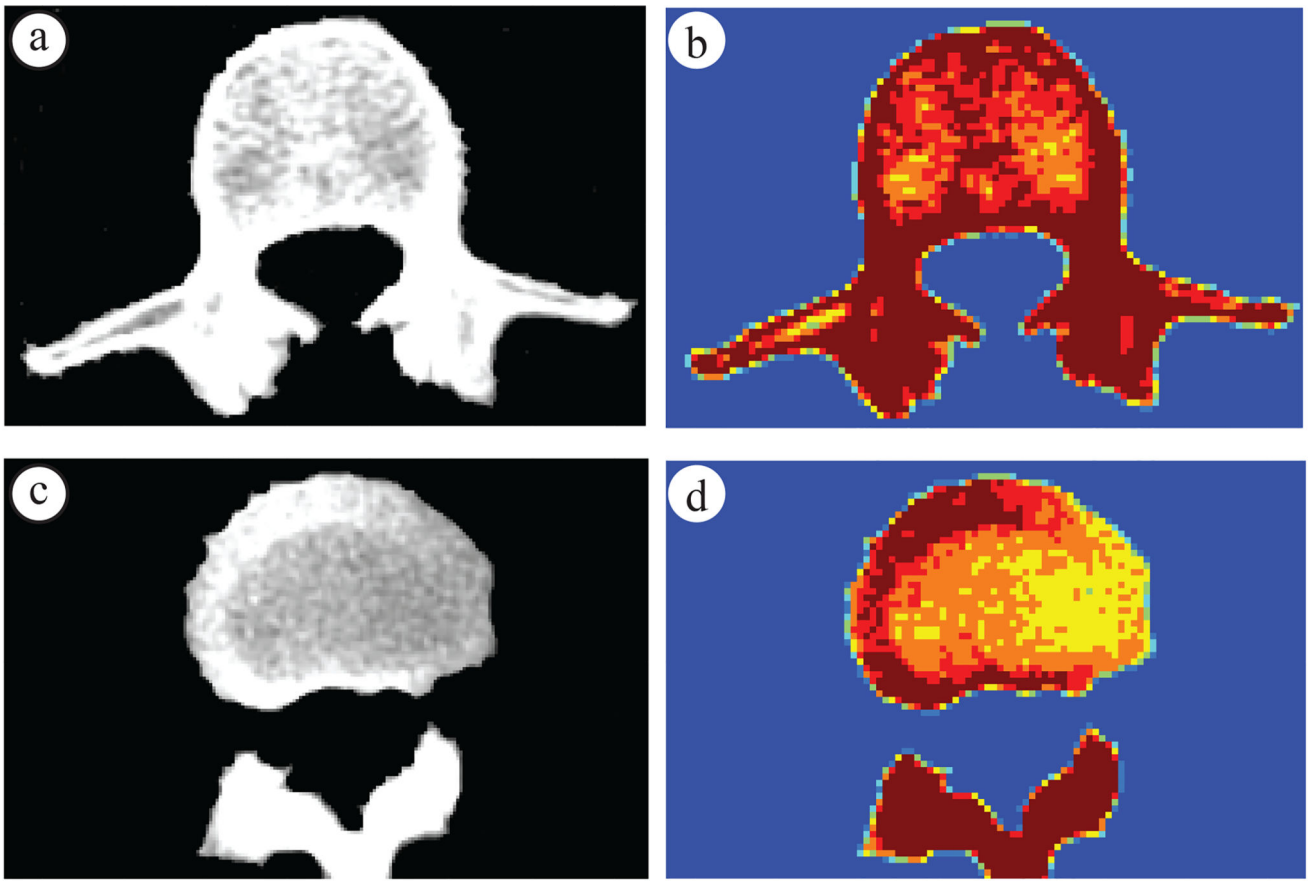

Fig. 7.

(a) First and (c) fourth images among the stack of four CT images of human vertebra and corresponding quantized images (b, d), respectively, at $l = 8$.

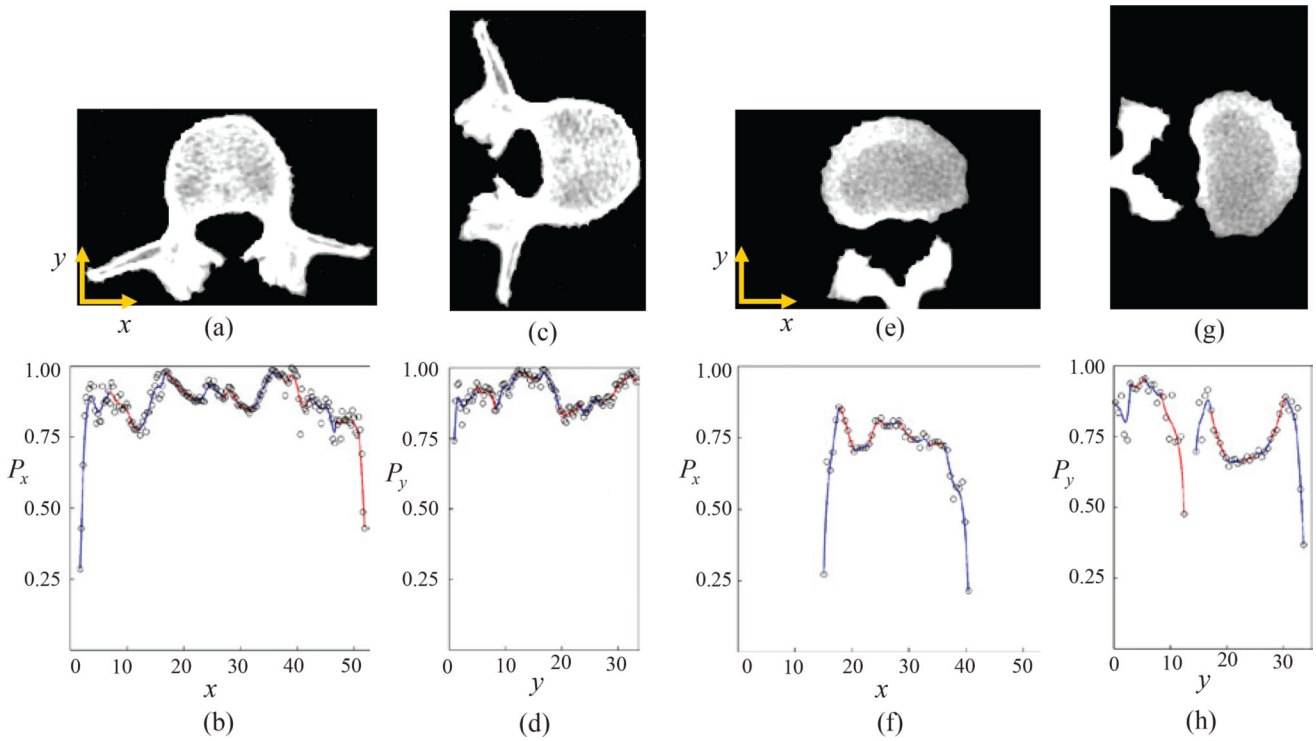

Fig. 8.

Two corresponding orthogonal topology function generated from first (a–d) and fourth (e–h) vertebra images (The image and functions are represented in the same scale).

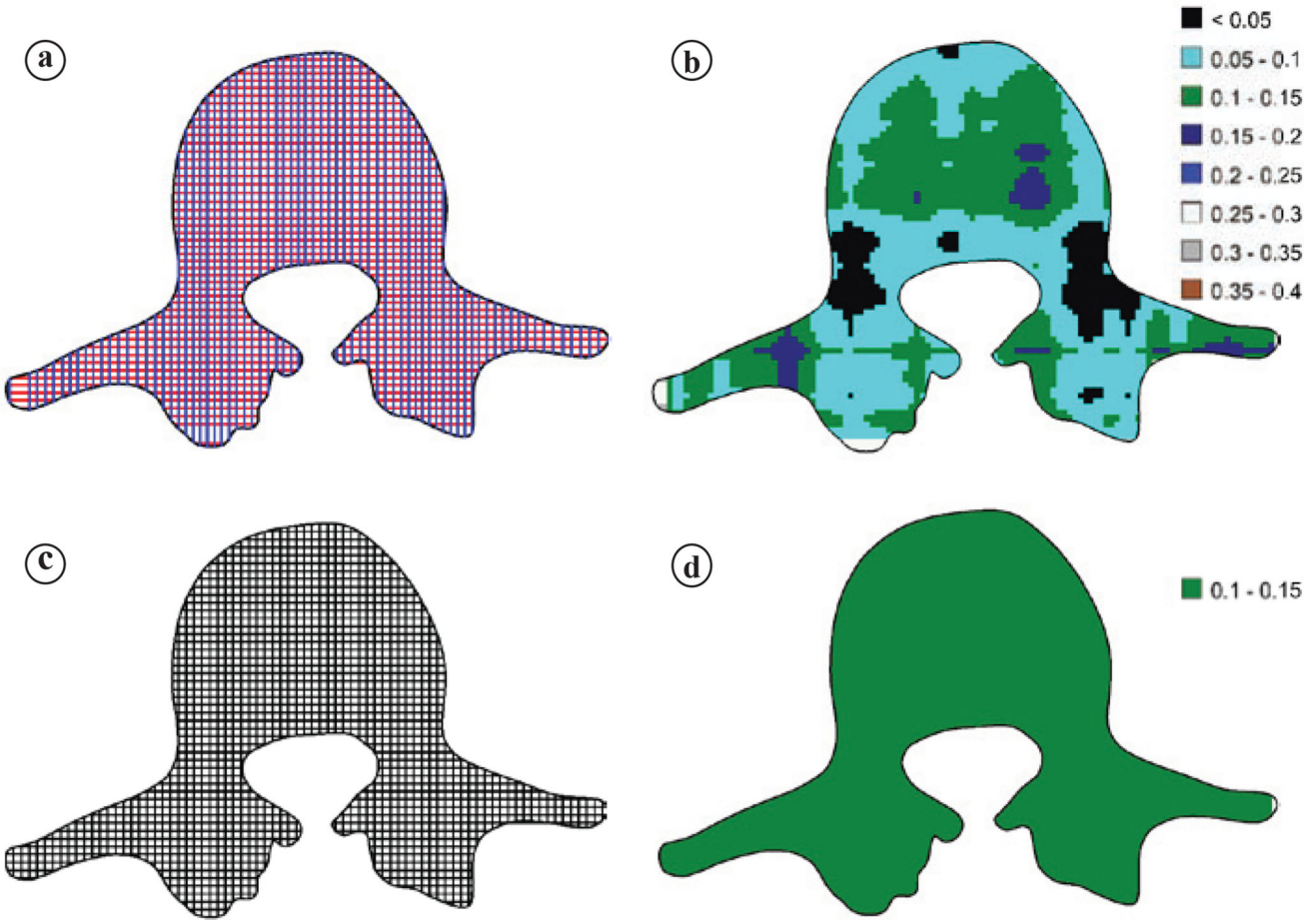

Fig. 9.

(a) Proposed variational porosity toolpath and (b) corresponding porosity distribution map for the first vertebra slice; (c) uniform porosity toolpath and (d) corresponding porosity distribution map for the first vertebra slice.

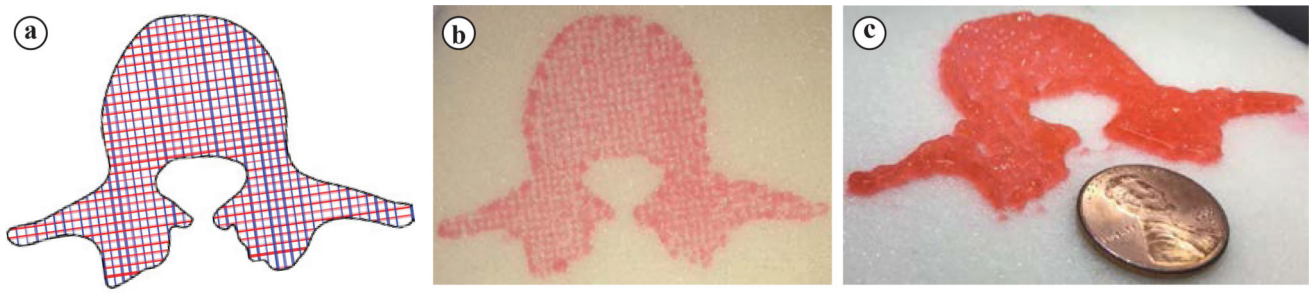

Fig. 10.

(a) Zigzag bi-layer toolpath for the first vertebra slice, (b) bio-printed bi-layer, and (c) bio-printed 10 layers vertebra.

Table 1

Comparison between the proposed method and the uniform porosity design.

	Avg. Percentage Error in Porosity	
	Proposed design	**Uniform porosity design**
Porosity	17.23%	23.41%

Table 2

Parameter comparison between the fabricated and designed layer.

Percentage Error in Fabricated part	
Filament Diameter (mm)	14.35%
Cell perimeter (mm)	7.73%
Porosity (%)	8.18%